



Mitigating indistinguishability issues in photon pair sources by delayed-pump intermodal four wave mixing

MASSIMO BORGHİ^{1,2,*}  AND LORENZO PAVESI¹ 

¹Nanoscience Laboratory, Department of Physics, University of Trento, Via Sommarive 14, 38123 Trento, Italy

²Present address: Department of Physics, University of Pavia, Via Agostino Bassi, 6, 27100 Pavia, Italy

*massimo.borghi@unipv.it

Abstract: Large arrays of independent, pure and identical heralded single photon sources are an important resource for linear optical quantum computing protocols. In the race towards the development of increasingly ideal sources, delayed-pump intermodal four wave mixing (IFWM) in multimode waveguides has recently emerged as one of the most promising approaches. Despite this, fabrication imperfections still spoil the spectral indistinguishability of photon pairs from independent sources. Here we show that by tapering the width of the waveguide and by controlling the delay between the pump pulses, we add additional spectral tunability to the source while still inheriting all the distinctive metrics of the IFWM scheme. This feature is used to recover spectral indistinguishability in presence of fabrication errors. Under realistic tolerances on the waveguide dimensions, we predict >99.5% indistinguishability between independent sources on the same chip, and a maximum degradation of the heralded Hong-Ou-Mandel visibility <0.35%.

© 2022 Optica Publishing Group under the terms of the [Optica Open Access Publishing Agreement](#)

1. Introduction

Spontaneous sources of photon pairs are primary resources in emerging large scale quantum photonic architectures, especially those based on integrated optics [1,2]. Through repeated application of heralding, large arrays of sources can be used to deterministically prepare many independent photons, which constitutes an important substrate for quantum information processing [3,4]. Their quality influences the ultimate computational power of the hardware, and limits the effective size of resources which are available for quantum algorithms and Linear Optical Quantum Computing architectures [5–7]. Two of the most relevant metrics are the purity and the indistinguishability of the heralded states [8]. In essence, they bound the visibility of multiphoton interference, which lies at the heart of protocols, algorithms and building blocks for quantum computation and quantum information. Examples include scattershot [9] and gaussian boson sampling [10], preparation of cluster states [11,12], realization of entangling gates [13,14] and state teleportation [15]. Several devices and methods have been developed to herald photons in pure states, characterized by a single and well defined spectral-temporal mode. These span from phase matching engineering [16], pump manipulation [17], selective control of the quality factor in microresonators [18] and spectral filtering [19]. Even if the purity can be improved from a clever design of the device, the indistinguishability relies exclusively on the fabrication uniformity of the array of sources. To date, even state of the art lithographic techniques can not guarantee sufficient uniformity levels, and errors must be compensated in post-fabrication. Indeed, the thickness uniformity of the silicon waveguide layer (long range disorder) has a rms value of 3 – 4 nm, while at die level ($\sim \text{cm}^2$ size, short range disorder), the uniformity in the waveguide width has an rms value <10 nm [20].

Independent sources based on microresonators can be made indistinguishable by aligning and locking their resonance wavelengths through thermo optic tuning [10,21]. However, this

method does not compensate slightly differences in the Free Spectral Range (FSR) or in the cavity linewidth, which are especially relevant for resonators of high quality factor. Waveguide sources without phase matching engineering emit photons in a broad spectral interval, and off or on-chip filters are used to increase their purity at the expense of reducing the heralding efficiency [22]. Therefore, the indistinguishability depends on the fabrication uniformity of the filters. In general, waveguide sources of spectrally uncorrelated photon pairs are not easily reconfigurable. Small tuning ranges can be obtained by heating the whole chip [23], while wider variations require to modify the pump wavelength [24]. Other techniques aim to erase the spectral distinguishability only after that the pair is generated. This can be achieved in materials with a strong second order nonlinearity by electro-optic frequency shearing [25], or in third order materials by Four Wave Mixing Bragg Scattering [26].

In this work, we propose and validate the design of a waveguide source which emits highly pure and spectrally tunable photons without spectral filtering. This is achieved through delayed-pump Intermodal Four Wave Mixing, a scheme recently reported on the Silicon On Insulator (SOI) platform which showed an heralded Hong Ou Mandel (HHOM) visibility of 96% between independent sources [27]. In contrast to the original work, we introduce an adiabatic change of the waveguide width along the propagation direction, and we tune the relative delay between the two pumps to reconfigure the phase matching wavelength of the emitted photons. The delay determines the point where the pump pulses overlap, which in turn selects the segment of the waveguide where pair generation occurs. Since the signal/idler frequencies depend on the waveguide cross-section, the delay reconfigures the generation wavelengths of the photon pair. We numerically investigate how this feature can be used to mitigate the distinguishability issues between different sources which arise from fabrication imperfections. We consider errors on both the waveguide width and height, focusing on realistic ranges provided by commercial foundries. We show that an indistinguishability level >95% can be guaranteed up to height differences of 4.3 nm, and for width differences greater than 100 nm. The HHOM visibility is shown to degrade by less than 0.35% from its value in two identical sources for devices on the same chip. In all the considered cases, the spectral tunability allows to dramatically improve the visibility of both Reverse (RHOM) and Heralded Hong Ou Mandel interference. We also prove that the principal source metrics and the spectral tunability are not degraded by the Self and the Cross Phase Modulation induced by the pump on the signal and the idler photon.

2. Principle of operation and theory

In spontaneous IFWM, photons from two bright pump fields (labeled as p_1 and p_2) annihilate to produce signal (s) and idler (i) photon pairs propagating in the different transverse modes of a multimode waveguide. The generation process occurs within narrow frequency ranges located at large spectral distances from the pump wavelength, where phase matching is satisfied [28]. By denoting the wavevectors of the fields as $(k_{p_1}, k_{p_2}, k_s, k_i)$, and their central wavelengths as $(\bar{\lambda}_{p_1}, \bar{\lambda}_{p_2}, \bar{\lambda}_s, \bar{\lambda}_i)$, this condition implies that $k_{p_1}(\bar{\lambda}_{p_1}) + k_{p_2}(\bar{\lambda}_{p_2}) = k_s(\bar{\lambda}_s) + k_i(\bar{\lambda}_i)$. The great flexibility offered by the choice of the modal combination and by the waveguide cross section has been exploited to tune the emission wavelengths from the Near Infrared to the Mid-Infrared [28,29] range. At the same time, the narrow generation bandwidth and the different group velocities of the modes can be exploited to engineer the emission of spectrally uncorrelated photon pairs. Within this framework, we revisit the configuration described in [27], where IFWM is demonstrated on a 220 nm thick SOI waveguide.

2.1. Tuning the phase matching wavelengths with the waveguide width

We use a Pump pulse of gaussian shape with a Full Width at Half Maximum (FWHM) duration of $T_0 = 0.8$ ps, a repetition rate of 50 MHz and a wavelength of 1550 nm. This is coupled in a coherent superposition of the two lowest order Transverse Magnetic (TM) modes (TM0 and

TM1 mode), with a relative delay τ between them. From now on, we will refer to the faster and delayed pulse in the TM0 mode as the pump p_1 , while the pulse in the TM1 mode as the pump p_2 . The multimode waveguide has a width of $\langle w \rangle = 2.25 \mu\text{m}$ and a length of $L = 1.5 \text{ cm}$. signal and idler photons are generated in the TM1 and TM0 modes respectively at the wavelengths $\lambda_s = 1581.4 \text{ nm}$ and $\lambda_i = 1519.9 \text{ nm}$. Geometrical variations with respect to this reference configuration lead to a shift $\Delta\lambda_{s(i)}$ of their phase matching wavelengths. This is shown in Fig. 1(a), in which $\Delta\lambda_s$ is plotted as a function of the deviation Δw and Δh in the waveguide width and height. Due to the remarked sensitivity of TM modes with the latter, we have that $\frac{d\lambda_s}{d\Delta h} \sim 1$ while $\frac{d\lambda_s}{d\Delta w} \sim -0.015$. Despite this, changing the waveguide width is easier than locally varying the thickness of the silicon device layer, so we can adjust Δw to tailor the emission wavelength of the source. We exploit two key characteristics of IFWM to realize a single device which can be reconfigured. The first is that due to the temporal walk-off between the pump pulses, the position $z = L_{\text{match}}$ along the waveguide where the pair generation probability is maximum depends on the delay τ . This is given by $L_{\text{match}} = \tau \left(\frac{1}{v_{p_2}} - \frac{1}{v_{p_1}} \right)$ (here, $v_{p_1} > v_{p_2}$ are the group velocities of pump p_1 and p_2), which is the coordinate where the two pump pulses overlap (see Appendix C). The effective width which determines the phase matching wavelengths corresponds to the local waveguide width $w(z)$ at position $z = L_{\text{match}}$. The second feature which we exploit is the fact that by letting w to vary along the propagation direction, the effective width where pair generation occurs can be controlled with τ . As a consequence, the generation wavelengths can be continuously tuned, as shown in Fig. 1(a). We focus on the configuration shown in Fig. 1(b), where the width of the waveguide is linearly tapered from $w(z=0) = \langle w \rangle + \Delta w$ to $w(z=L) = \langle w \rangle - \Delta w$, with $\Delta w \geq 0$. We define $\tau_{\text{max}} = 4.9 \text{ ps}$ as the delay which makes the two pump pulses to overlap at the end of the waveguide. In Fig. 1(b) we analyze three extremal cases. When $\tau = 0$, the maximum pump overlap occurs at $\langle w \rangle + \Delta w$, and according to Fig. 1(a), $\Delta\lambda_s < 0$, i.e., pairs are generated at wavelengths closer to the one of the pump. When $\tau = \frac{\tau_{\text{max}}}{2}$, the overlap is maximum at $\langle w \rangle$, and the phase matching wavelengths are not changed with respect to the case $\Delta w = 0$. When $\tau = \tau_{\text{max}}$, the pump pulses catch at the narrower end of the waveguide, and photon pairs are generated at larger spectral detunings with respect to the pump wavelength. As long as L exceeds the walk-off length between the pump pulses, and that the choice of τ allows a complete progression of one pulse over the other, the generation bandwidth and the efficiency remains constant. In the next section, we quantitatively evaluate $\Delta\lambda_{s(i)}$ as a function of τ and Δw , focusing on how the pair generation probability and the purity of the heralded single photon states are affected.

2.2. Theory of photon pair generation in the tapered source

The spectral (temporal) properties of photon pairs are characterized their Joint Spectral (Temporal) Amplitude (JSA/JTA), and most of the source metrics can be derived from this function [30]. We then focus on the derivation of the JSA/JTA, taking into account the multiple spatial modes in the FWM process, the delayed pump configuration, the varying waveguide width along the propagation direction and the effects of SPM and XPM between the pumps and the signal/idler photons. The electric fields of the two pumps $p = \{p_1, p_2\}$ are treated classically and are expressed as [31]:

$$\mathbf{E}_p(z, t) = \frac{1}{2} \mathbf{e} F_p(x, y) \sqrt{\frac{2}{n \epsilon_0 c}} \tilde{A}_p(z, t) e^{i(\tilde{\beta}_p z - \tilde{\omega}_p t)} + \text{c.c.}, \quad (1)$$

where \mathbf{e} is the unit vector of polarization, F_p is the transverse mode profile (normalized such that $\int |F_p(x, y)|^2 dx dy = 1$), n is the refractive index of the waveguide core, $\tilde{\beta}_p$ and $\tilde{\omega}_p$ the central wavevector and frequency of the fields, and \tilde{A}_p a slowly varying envelope function. The power carried by the field in Eq. (1) is $P_p = |\tilde{A}_p|^2$, as can be verified by integrating the Poynting vector

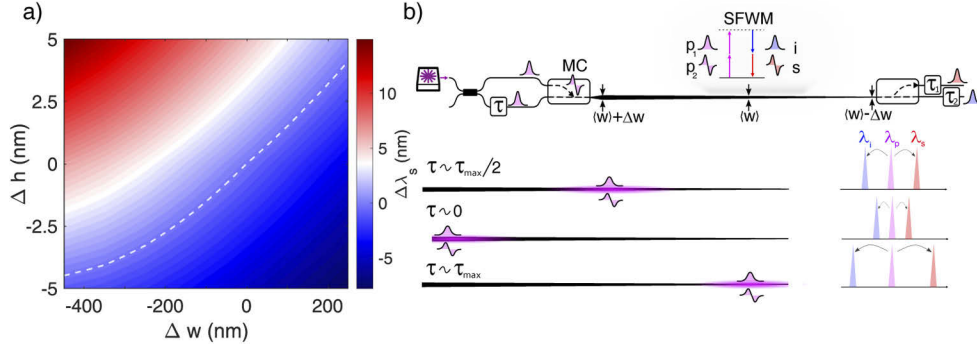


Fig. 1. (a) Variation of the phase matching wavelength of the signal $\Delta\lambda_s$ with respect to changes in the width (Δw) and height (Δh) of the reference waveguide cross-section $2.25 \times 0.22 \mu\text{m}$. The white dashed line follows $\Delta\lambda_s = 0$. (b) Top: sketch of the source, with indicated the relevant components and parameters (MC = Mode Converter). Bottom: principle of operation of the tunable source. In order to tune the phase matching wavelengths of the signal (λ_s) and of the Idler (λ_i) (right sketch), the two pump pulses are delayed by a variable amount of time τ , making them to overlap in different positions (magenta color) along the waveguide. At each delay, a different waveguide width is sensed, and the phase matching wavelengths change according to panel (a). The delays τ_1 and τ_2 are respectively applied to the signal and the idler photon to control their arrival time.

$\mathbf{S} = \frac{\mathbf{E} \times \mathbf{B}}{\mu_0}$ across the waveguide cross section. The two pump envelopes are temporally delayed gaussians, and are defined in Appendix C. The signal and the idler fields are quantized as:

$$\mathbf{E}_{s(i)}(z, t) = \frac{1}{2} \mathbf{e} F_{s(i)}(x, y) \frac{1}{2\pi} \int \sqrt{\frac{2\hbar\omega}{n\epsilon_0 c}} \tilde{a}_{s(i)}(z, \omega) e^{-i\omega t} e^{i(\tilde{\beta}_{s(i)}z - \tilde{\omega}_{s(i)}t)} d\omega + \text{c.c.}, \quad (2)$$

where $\tilde{a}_{s(i)}(z, \omega)$ represents the Fourier Transform of the slowly varying annihilation operator $\tilde{a}_{s(i)}(z, t)$ for the signal(idler) photon. It is possible to formally derive the propagation equation for $\mathbf{E}_{p_1(2)}$ in a fully quantum mechanical framework by treating $\tilde{A}_{p_1(2)}$ as an operator and by using the Heisenberg equation of motion. However, we anticipate the result of the classical regime, in line with the fact that the field in Eq. (1) is not quantized. This is given by the well known set of coupled Nonlinear Schrodinger equations (NLSE) [32]:

$$\frac{\partial \tilde{A}_{p_1}}{\partial z} = \left(-\frac{\alpha_{p_1}}{2} + i\Delta\beta_{p_1}(z) - \frac{i}{2L_{D_{p_1}}} \frac{\partial^2}{\partial T^2} \right) \tilde{A}_{p_1} + i \left(2\gamma_{1122} |\tilde{A}_{p_2}|^2 + \gamma_{1111} |\tilde{A}_{p_1}|^2 \right) \tilde{A}_{p_1}, \quad (3)$$

$$\frac{\partial \tilde{A}_{p_2}}{\partial z} = \left(-\frac{\alpha_{p_2}}{2} + i\Delta\beta_{p_2}(z) - \frac{i}{2L_{D_{p_2}}} \frac{\partial^2}{\partial T^2} - \frac{1}{L_{w_p}} \frac{\partial}{\partial T} \right) \tilde{A}_{p_2} + i \left(2\gamma_{2211} |\tilde{A}_{p_1}|^2 + \gamma_{2222} |\tilde{A}_{p_2}|^2 \right) \tilde{A}_{p_2}, \quad (4)$$

where the dimensionless time $T = \left(t - \frac{z}{v_{g1}} \right) / T_0$ refers to a reference frame moving at the group velocity of pump p_1 . The definition of the parameters can be found in Appendix A. The second term on the right hand side of Eq. (3,4) is defined as $\Delta\beta_p = \beta_p(z, \tilde{\omega}_p) - \tilde{\beta}_p$, and accounts for the varying waveguide width along the propagation direction. Consistently with the framework of the slowly varying envelope approximation, we neglected in Eq. (3) the term proportional to $\frac{\partial \tilde{\beta}}{\partial z}$. This is justified from the fact that the wavevector $\beta(z)$ varies on a scale ($\sim \text{cm}$) which is much larger than the size of the field envelope ($\sim 100 \mu\text{m}$) [33]. We numerically integrated this set of equations using a third order, symmetrized Split-Step Fourier method (SSFM) [34]. To

obtain a similar set of equations for the signal and the idler field operators, we use the Heisenberg equation of motion generated by the momentum operator $M(z, t)$, which is $-i\hbar \frac{dO}{dz} = [O, M]$ [35], where O is any operator in the Heisenberg picture. The total momentum can be written as $M = M_L + M_{\text{SPM}} + M_{\text{XPM}} + M_{\text{FWM}}$, which is the sum of the linear, the SPM, the XPM and the FWM induced momentum [36], and whose expressions can be found in Appendix A. We then move in the interaction picture and split the total momentum into $M = M_0 + M_{\text{FWM}}$, where all the trivial evolution is generated by $M_0 = M_L + M_{\text{SPM}} + M_{\text{XPM}}$. The pair generation process is described by the interaction momentum M_{FWM} . Using the expressions for M_L , M_{SPM} and M_{XPM} provided in Appendix A, and the equal position commutation relation $[\tilde{a}(z, t), \tilde{a}^\dagger(z, t')] = \delta(t - t')$ [31], we get [37]:

$$\frac{\partial \tilde{a}_q}{\partial z} = \left(-\frac{\alpha_q}{2} + i\Delta\beta_q(z) - \frac{i}{2L_{D_q}} \frac{\partial^2}{\partial T^2} - \frac{1}{L_{w_q}} \frac{\partial}{\partial T} \right) \tilde{a}_q + 2i \left(\gamma_{11qq} |\tilde{A}_{p_1}|^2 + \gamma_{22qq} |\tilde{A}_{p_2}|^2 \right) \tilde{a}_q, \quad (5)$$

where $q = \{s, i\}$ labels the signal or the idler, and we have neglected their XPM and SPM. It is worth to note that losses have been phenomenologically introduced by the linear loss coefficients α_q . Losses spoil the photon number correlation between the signal and the idler photon in the two-mode squeezed state generated by M_{FWM} , which could be accounted by introducing a reservoir of loss modes that is coupled to the signal/idler fields [38]. Beside that, the simultaneous presence of squeezing and loss differs from the case where the two effects separately act [38]. However, the latter well approximates the case of IFWM, since the interaction length is small compared to the one of the waveguide, and losses can be assumed to be all localized after that pair generation is occurred. As an upper estimate, we will show later that the interaction length is of the order of $0.2L$, and by considering a propagation loss of 0.4 dB/cm (see Table 1 and [27]) this gives ~ 0.16 dB. Provided that we restrict our attention to the low squeezing regime of single pair generation, the loss term in Eq. (5) simply scales the pair generation probability by a factor $\alpha_s \alpha_i$, and does not contribute to modify the shape of the JSA. The state $|\Psi(z)\rangle$ of the signal and the idler photon, lying in vacuum at $z = 0$, evolves as $-i\hbar \frac{d|\Psi\rangle}{dz} = M_{\text{FWM}}|\Psi\rangle$ [36], and its solution can be formally written in terms of a space propagator $|\Psi(z)\rangle = U(z, 0)|\Psi(0)\rangle$ [31]. In the regime of single pair generation, this is given by $U(z, 0) = I + \frac{i}{\hbar} \int_0^z M_{\text{FWM}}(z') dz'$, where I denotes the identity operator. From the two-photon state, we can define the joint amplitude probability $\Phi(T_s, T_i, z)$ of detecting, at position z , the signal photon at time T_s and the idler photon at time T_i , as $\Phi(T_s, T_i, z) = \langle \tilde{a}_s(T_s, z) \tilde{a}_i(T_i, z) U(z, 0) \rangle$, where the expectation value is evaluated on vacuum. When Φ is normalized such that $\int |\Phi|^2 dT_s dT_i = 1$, this coincides with the definition of the JTA [37]. In the rest of the paper, we will refer to $\Phi(T_s, T_i, z)$ as the JTA without distinction. The JSA $\Phi(\omega'_s, \omega'_i, z)$, expressed in the dimensionless frequencies $\omega'_{s(i)} = (\omega_{s(i)} - \bar{\omega}_{s(i)})T_0$, is related to $\Phi(T_s, T_i, z)$ by a two-dimensional Fourier Transform [36]. Following the derivation detailed in Appendix B, and similarly reported in [39], we can write a propagation equation for the JTA. By expressing the latter as $\Phi = \tilde{\Phi}(T_s, T_i, z) e^{i\Theta_{si}(z)}$, where $\Theta_{si} = \int_0^z (\Delta\beta_s(z') + \Delta\beta_i(z')) dz'$, the function $\tilde{\Phi}$ obeys the equation:

$$\frac{\partial \tilde{\Phi}(T_s, T_i, z)}{\partial z} = (L_s + L_i + N_s + N_i) \tilde{\Phi}(T_s, T_i, z) + S(T_s, T_i, z), \quad (6)$$

where the operators L_q, N_q ($q = \{s, i\}$) and the driving term S are defined as:

$$\begin{aligned}
 L_q &= -\frac{\alpha_q}{2} - \frac{1}{L_{w_q}} \frac{\partial}{\partial T_q} - \frac{i}{2L_{D_q}} \frac{\partial^2}{\partial T_q^2}, \\
 N_q &= 2i(\gamma_{11qq} |\tilde{A}_{p1}(z, T_q)|^2 + \gamma_{22qq} |\tilde{A}_{p2}(z, T_q)|^2), \\
 S &= \gamma_{p1p2si} e^{i\Theta(z)} \int G(\omega'_s, \omega'_i, z) e^{-i(T_s \omega'_s + T_i \omega'_i)} d\omega'_s d\omega'_i, \\
 G(\omega'_s, \omega'_i, z) &= i \int \tilde{\mathcal{A}}_{p1}(x, z) \tilde{\mathcal{A}}_{p2}(\omega'_s + \omega'_i - x, z) dx, \\
 \Theta(z) &= \int_0^z (\Delta\beta_{p1}(z') + \Delta\beta_{p2}(z') - \Delta\beta_s(z') - \Delta\beta_i(z')) dz',
 \end{aligned} \tag{7}$$

where we wrote the Fourier Transform of $\tilde{A}_{p1(2)}(z, T)$ as $\tilde{\mathcal{A}}_{p1(2)}(z) \exp \left[i \int_0^z \Delta\beta_{p1(2)}(z') dz' \right]$ to factor out the accumulated phase due to the tapering. Equation (6) has the same structure of a two-dimensional NLSE in the dimensionless time variables (T_s, T_i), with the inclusion of an external driving term S .

3. Analysis of the source performance

Using the third order SSFM developed in [31,39], we numerically integrated Eq. (6) to calculate the JTA and the JSA for different tapering amplitudes Δw and for different delays τ . The average pump power is set to 1 mW, and is equally distributed between the TM0 and the TM1 modes. The mean wavelength shift $\Delta\lambda_s$ of the signal photon, calculated from the JSA, is shown in Fig. 2(a), while the related JSAs (plotted here only for $\Delta w = 0.25 \mu\text{m}$) are shown in Fig. 2(b). For a fixed value of Δw , the phase matching wavelengths are continuously tuned with τ . The trends follow the one indicated in Fig. 1(a,b), where the spectral separation of the signal/idler wavelengths monotonically increases as $\tau \rightarrow \tau_{\text{max}}$. The maximum tuning range depends on Δw , and increases

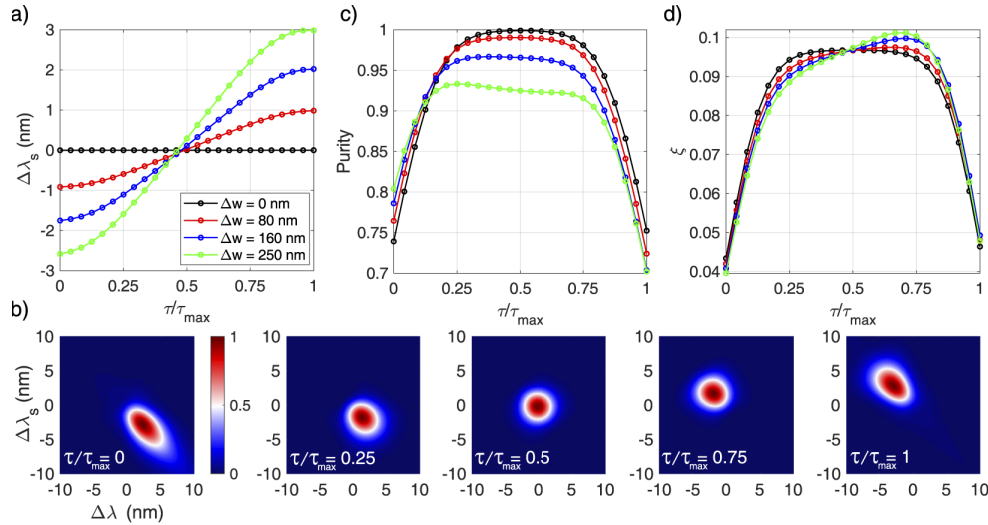


Fig. 2. (a) Relative shift of the average signal wavelength as a function of the time delay τ between the pumps. Different curves refer to different tapering amplitudes Δw . (b) JSA of the photon pair source for different choices of the delay τ . The tapering amplitude is fixed to $\Delta w = 0.25 \mu\text{m}$. (c) Purity of the heralded photon states as a function of the delay τ and for different values of Δw . (d) Same as in (c), but relative to the pair generation probability ξ .

from $\Delta\lambda_s^{\max} = \Delta\lambda_s(\tau = \tau_{\max}) - \Delta\lambda_s(\tau = 0) \sim 2$ nm for $\Delta w = 0.08 \mu\text{m}$ to $\Delta\lambda_s^{\max} \sim 6.5$ nm for $\Delta w = 0.25 \mu\text{m}$. Except for the extremal cases $\tau = \{0, \tau_{\max}\}$, the JSA maintains an almost perfect circular shape. As long as the tapering angle $2\Delta w/L$ is kept shallow, the local waveguide width does not appreciably change along the interaction length, and the generation bandwidth remains constant. The high purity of the signal and the idler photon is shown in Fig. 2(c). With respect to the a straight waveguide ($\Delta w = 0$), for which the purity is maximum and equal to $\mathcal{P} = 0.998$ at $\tau = 0.5\tau_{\max}$, this only decreases to $\mathcal{P} = 0.98$ for $\Delta w = 0.08 \mu\text{m}$ and to $\mathcal{P} = 0.91$ for $\Delta w = 0.25 \mu\text{m}$. The decrease of the purity is associated to the broadening of the signal/idler spectra as the tapering becomes more aggressive. This could be mitigated by increasing the waveguide length or by decreasing the interaction length by reducing the temporal duration of the pump pulse. The pair generation probability ξ is almost not affected by Δw . As $\tau \rightarrow \tau_{\max}$, the sensed effective area becomes smaller, but this does not improve the FWM strength since the two pump pulses accumulate more losses before overlapping at the narrower end of the waveguide. The source metrics discussed so far refer to the properties of the signal/idler pair at the end of the waveguide, but they do not offer a physical insight into the evolution of the two-photon state as it propagates along the source. One of the strengths of Eq. (6) is to provide a natural framework to track evolution of any metric along the waveguide. As an example, the accumulated pair generation probability $\xi(z) = \int |\Phi(T_s, T_i, z)|^2 dT_s dT_i$, from the beginning of the waveguide to position z , can be computed starting from Eq. (6) as:

$$\xi(z) = \int \left(\int_0^z \left(-(\alpha_s + \alpha_i) |\Phi(T_s, T_i, z')|^2 + 2\Re [S\Phi(T_s, T_i, z')^*] \right) dz' \right) dT_s dT_i, \quad (8)$$

where \Re denotes the real part and we have used the fact that, from Eq. (7), $L_{s(i)}^\dagger = -L_{s(i)} + \alpha_{s(i)}$ and $N_{s(i)}^\dagger = -N_{s(i)}$. In Fig. 3(a), we plot ξ as a function of z for $\frac{\tau}{\tau_{\max}} = \{0.25, 0.5, 0.75\}$ and $\Delta w = 0.1 \mu\text{m}$. The essence of IFWM emerges from these curves. The generation probability is approximately zero until $\frac{z}{L} \sim \frac{\tau}{\tau_{\max}}$, which is the point where the two pump pulses match.

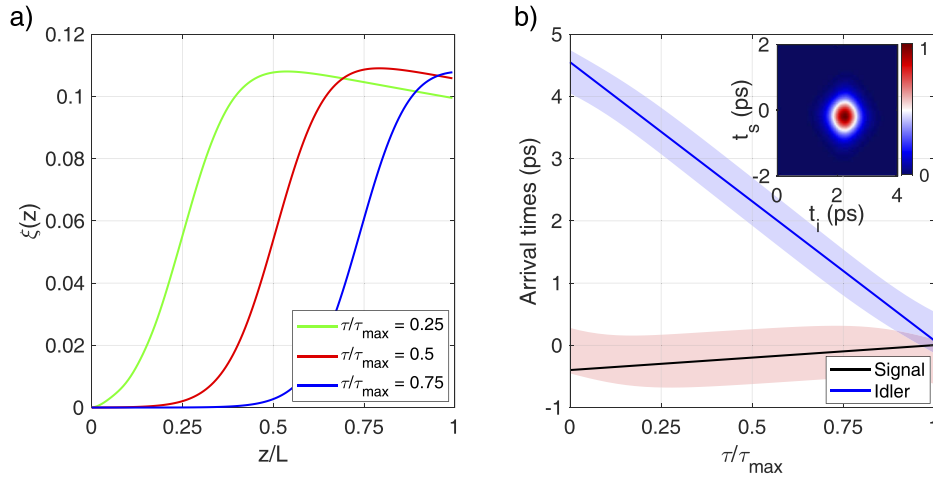


Fig. 3. (a) Cumulative photon pair generation probability ξ as a function of the position z along the waveguide. Different curves refer to different choices of the relative pump delay τ . (b) Average arrival times of the signal (black) and of the idler (blue) photon at the end of the waveguide, calculated using Eq. (9). These values are relative to the arrival time of the pump pulse which lies in the TM0 mode. The inset shows an example of the JTA for $\frac{\tau}{\tau_{\max}} = 0.5$, from which the mean $\langle T_{s(i)} \rangle$ and the standard deviation $\sigma_{T_{s(i)}}$ on the arrival times are extracted. These are plotted as shaded regions ($\langle T_{s(i)} \rangle \pm \sigma_{T_{s(i)}}$).

Then, the value of ξ smoothly grows from the 5% to the 95% of its maximum in a length of $L_{\text{grow}} \sim 0.36L$. Then, the cumulative generation probability saturates since the pump pulses lose their spatial overlap, and after that it exponentially decays due to the propagation losses. As shown in Appendix C, the function $\xi(z)$ can be approximated by an *erf* function, which implies that its derivative, representing the pair generation probability per unit length, is a gaussian peaked at $\frac{z}{L} = \frac{\tau}{\tau_{\text{max}}}$. Its FWHM Δ_z can be assessed from $\Delta_z = \frac{\ln(2)}{2} L_{\text{grow}} \sim 0.21L$. This value is very close to the approximated analytic result found in Appendix C, which is $\Delta_z = \sqrt{2} L_{w_p} = 0.20L$. For $\Delta w = 0.1 \mu\text{m}$, the width of the waveguide changes by $\frac{2\Delta w \Delta_z}{L} \sim 0.06 \mu\text{m}$ along Δ_z , which is the $\sim 2.5\%$ of the waveguide width. The arrival times of the signal and the idler photon at the end of the waveguide can be inferred from the JTA shown in the inset of Fig. 3(b). Photons are generated in a well defined gaussian temporal wavepacket, whose size is of the same order of the pump duration (0.8 ps). From the JTA, the mean and the standard deviation on the signal/idler arrival times are calculated, which are shown in Fig. 3(b) (shaded regions) as a function of τ and for $\Delta w = 0$. These values are relative to the arrival time of the faster pump pulse, in accordance to the fact that Eq. (7) is expressed in a moving reference frame. The arrival times can be analytically predicted by assuming that the pair is generated at the position where the two pump pulses have their maximum overlap, which for a delay τ occurs at $z = L_{\text{match}} = \frac{\tau T_0}{L_{w_p}}$. From $z = L_{\text{match}}$, the time required for the signal (idler) photon to reach the end of the waveguide is $\frac{L - L_{\text{match}}}{v_{s(i)}}$, from which is easy to show that the arrival times $\mathcal{T}_{s(i)}$ are given by:

$$\mathcal{T}_{s(i)} = \frac{1}{|L_{w_{s(i)}}|} \left(\pm L_{w_p} \tau \mp T_0 L \right), \quad (9)$$

where the + sign is used for the signal. The solid lines in Fig. 3(b), obtained from Eq. (9), show a good agreement with the arrival times calculated from the JTA.

4. Mitigating indistinguishability issues in two photon interference

We now exploit the tunability of the source to mitigate the indistinguishability issues which arise from fabrication imperfections in independent devices. Suppose to have two sources, labelled 1 and 2, which can either lie on the same die or on two different chips. In general, due to fabrication imperfections, they will have a different cross-section and JSA, which will compromise their capability to interfere. We can try to recover their spectral indistinguishability by respectively applying pump delays τ_1 and τ_2 to the two sources in order to overlap their signal/idler spectra. Unfortunately, as shown in Fig. 3(b), whenever $\tau_1 \neq \tau_2$, the signal(idler) photons will arrive at the end of the waveguide at the different times $\tau_{s1}(\tau_{i1})$ and $\tau_{s2}(\tau_{i2})$. In other terms, they will be spectrally indistinguishable but temporarily distinguishable. In order to erase the temporal information, additional delay stages have to be placed at the end of the waveguide, which make $\tau_{s1}(\tau_{i1}) = \tau_{s2}(\tau_{i2})$. To this purpose, the same component used to delay the pump pulses can be implemented, as shown in Fig. 1(b). We numerically investigated the maximum visibility of two photon interference that can be obtained for increasing amounts of fabrication error. We focused on two key experiments, which are respectively based on the RHOM and on the HHOM effect. In RHOM, the two-photon states $|\Pi_{1(2)}\rangle = \int \Phi_{1(2)}(\omega_s, \omega_i) a_s^\dagger(\omega_s) a_i^\dagger(\omega_i) |0\rangle$ generated by source 1 and 2 are sent at the input ports *a* and *b* of a balanced beamsplitter, in the coherent superposition $|\Psi\rangle = \frac{1}{\sqrt{2}} (|\Pi\rangle_{1,a} + e^{i\theta} |\Pi\rangle_{2,b})$. Coincidences are monitored between the output ports as a function of θ . It can be demonstrated that the visibility $\mathcal{V}_{\text{RHOM}}$ of the two-photon fringe coincides with the indistinguishability [27], i.e.:

$$\mathcal{V}_{\text{RHOM}} = \left| \int \Phi_1(\omega_s, \omega_i) \Phi_2^*(\omega_s, \omega_i) d\omega_s d\omega_i \right|^2. \quad (10)$$

In the case of HHOM, in each source we use one photon of the pair, say the idler, to herald its partner. Among the heralded signals, one is delayed with respect to the other, after that the two are interfered at the input ports of a 50/50 beamsplitter. A dip in the coincidences between the photons emerging at the output ports is observed at zero delay, with visibility [40]:

$$\mathcal{V}_{\text{HHOM}} = \left| \int dT_s dT'_s (\Phi_1(T_s, T_i) \Phi_1^*(T'_s, T_i) dT_i) (\Phi_2(T'_s, T'_i) \Phi_2^*(T_s, T'_i) dT'_i) \right|. \quad (11)$$

This quantity depends on both the indistinguishability and the purity of the heralded photons. Figure 4(a) shows the maximum values of $\mathcal{V}_{\text{RHOM}}$ and $\mathcal{V}_{\text{HHOM}}$ which can be achieved after optimization of τ_1 and τ_2 . The quantities are shown as a function of the height difference $|h_1 - h_2|$ of the two waveguides sources, which are assumed to have the same average width $\langle w \rangle = 2.25 \mu\text{m}$ and tapering $\Delta w = 0.25 \mu\text{m}$. In the optimization procedure, the temporal distinguishability is erased in two steps. First, we compute the mean arrival times $(\tau_{s1(2)}, \tau_{i1(2)})$ of each photon from the JTAs $\Phi_{1(2)}$. Second, the JTA of source 2 is shifted in time as $\Phi_2(T_s, T_i) \rightarrow \Phi(T_s + (\tau_{2s} - \tau_{1s}), T_i + (\tau_{2i} - \tau_{1i}))$ to mimic the presence of a delay stage on the path of each photon. Using the JTA of source 1 and the delayed JTA of source 2, the visibilities are computed according to Eq. (10–11). From Fig. 4(a), we see that $\mathcal{V}_{\text{RHOM}}$ is higher than 0.95 for $|h_2 - h_1| \leq 4.3 \text{ nm}$, while in the same range $\mathcal{V}_{\text{HHOM}} \geq 0.9$, which is only 3% less than its value at $|h_2 - h_1| = 0$ ($\mathcal{V}_{\text{HHOM}} = 0.93$). On the contrary, both $\mathcal{V}_{\text{RHOM}}$ and $\mathcal{V}_{\text{HHOM}}$ rapidly decrease to zero if the delays are not optimized. As shown in the inset of Fig. 4(a), we have that 1 nm of error in the waveguide height is sufficient to drop $\mathcal{V}_{\text{RHOM}}$ to 0.89 and $\mathcal{V}_{\text{HHOM}}$ to 0.81, while their values are almost unaffected ($\mathcal{V}_{\text{RHOM}} > 0.995$, $(\mathcal{V}_{\text{HHOM}}(h_1 = h_2) - \mathcal{V}_{\text{HHOM}}(\Delta h = 1 \text{ nm})) / \mathcal{V}_{\text{HHOM}}(h_1 = h_2) < 0.35\%$) in the optimized case. This range is especially relevant for sources which lie on the same die, for which the thickness uniformity of the silicon device layer is sub-nm [20]. When the fabrication error is considered on the average waveguide width $\langle w \rangle$ (assuming the same height for both sources), a similar result is found, as shown in Fig. 4(b). As already discussed in Section 2, the phase matching wavelengths are less affected by variations of the waveguide width. As a consequence, a small tapering amplitude, with $\Delta w = 0.1 \mu\text{m}$ in Fig. 4(b), is sufficient to recover the indistinguishability. As an example, for $|\langle w_1 \rangle - \langle w_2 \rangle| \leq 60 \text{ nm}$, we have that $\mathcal{V}_{\text{RHOM}} \geq 0.995$ and $\mathcal{V}_{\text{HHOM}} \geq 0.98$. Without delay optimization, for $|\langle w_1 \rangle - \langle w_2 \rangle| = 60 \text{ nm}$ their value drop to $\mathcal{V}_{\text{RHOM}} = 0.92$ and $\mathcal{V}_{\text{HHOM}} = 0.88$. The inset in Fig. 4(b) shows that for errors in the waveguide width below 15 nm, which is a meaningful range for sources lying on the same die [20,41], the optimized values of $\mathcal{V}_{\text{RHOM}}$ and $\mathcal{V}_{\text{HHOM}}$ are almost equal to the case of identical waveguides. In Fig. 4(c) we report the values of τ_1 and τ_2 which maximize the fringe visibility as a function of the error on the average waveguide width. As the latter increases, τ_1 and τ_2 show opposite trends. From the trivial case $\tau_1 = \tau_2 = \frac{\tau_{\text{max}}}{2}$, which occurs at $\langle w_1 \rangle = \langle w_2 \rangle$, we have that by increasing the difference in the waveguide width, τ_1 monotonically decreases while τ_2 increases (we arbitrarily choose $\langle w_1 \rangle \leq \langle w_2 \rangle$ to fix the sign of $\Delta\lambda_s$, the behaviour will be inverted in the opposite case). To intuitively understand this trend, suppose that due to an error on the waveguide width, sources 1 and 2 emit pairs with a wavelength difference $\Delta\lambda_{s(i)} = \lambda_{s(i)1} - \lambda_{s(i)2}$. We could recover the spectral indistinguishability by acting exclusively on the delay of source 1, i.e., $\tau_1 \rightarrow \frac{\tau_{\text{max}}}{2} \pm \Delta\tau$, where the choice of the sign depends on the one of $\Delta\lambda_s$ (equivalently $\Delta\lambda_i$). However, Fig. 2(b) indicates that at both large and small delays, the shape of the JSA is asymmetric, and the purity of the heralded single photon states decreases with respect to $\tau = \frac{\tau_{\text{max}}}{2}$. It is then more convenient to modify the delay of both sources, choosing $\tau_1 \sim \frac{\tau_{\text{max}}}{2} \pm \frac{\Delta\tau}{2}$ and $\tau_2 \sim \frac{\tau_{\text{max}}}{2} \mp \frac{\Delta\tau}{2}$, rather than imparting the whole delay $\Delta\tau$ on source 1. In this way, the JSA of both sources will have less distortions.

We evaluated that in order to compensate for silicon device thickness inhomogeneities $\leq 1 \text{ nm}$ the delay must be tunable in the range $0.35\tau_{\text{max}} \leq \tau \leq 0.65\tau_{\text{max}}$, which corresponds to $1.71 \text{ ps} \leq \tau \leq 3.18 \text{ ps}$. With reference to the device sketched in Fig. 1(b), this could be achieved

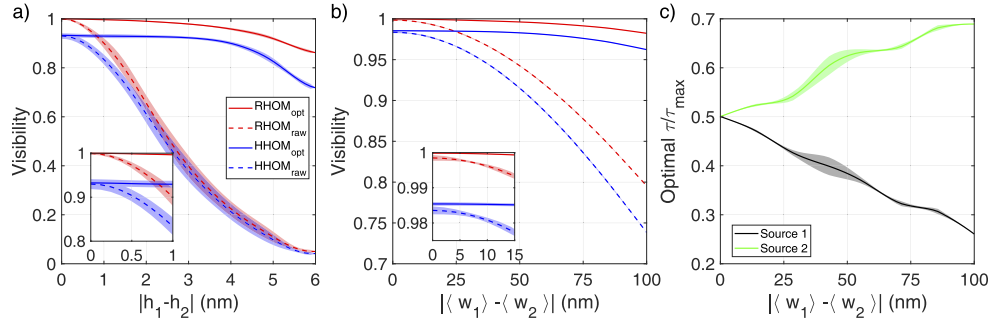


Fig. 4. (a) RHOM and HHOM visibilities as a function of the height difference of the two waveguide sources in the delay-optimized (RHOM_{opt}, HHOM_{opt}) and not optimized (RHOM_{raw}, HHOM_{raw}) cases. The inset shows a detail of the region $|h_1 - h_2| \leq 1$. Visibilities \mathcal{V} are calculated in the two dimensional grid spanned by h_1 and h_2 , which are stored in the matrix \mathcal{V}_{ij} . From this matrix, we calculated the mean and the standard deviation on \mathcal{V} as a function of the absolute height difference $|h_1 - h_2|$ by tracing along the anti-diagonal lines. The shaded regions cover one standard deviation on \mathcal{V} . (b) Same as in (a), but the visibilities are shown for a fixed thickness of the waveguide (220 nm) and as a function of the difference on the average waveguide width between the sources. (c) Values of the delays τ_1 (black, relative to source 1) and τ_2 (green, relative to source 2) which maximize the visibility in panel (b).

by placing a delay line in the lower arm after the input beamsplitter, which is reconfigurable in the range $\Delta\tau = \tau_0 \pm \frac{\Delta T}{2}$, where τ_0 is a bias delay and $\Delta T = (3.18 - 1.71) = 1.47$ ps. When the delay line is set into its rest state ($\Delta\tau = \tau_0$), the length difference between the lower and the upper arm after the input beamsplitter must be $\Delta L = v_{p1}(\frac{\tau_{\max}}{2} - \tau_0)$. Among the different devices which can physically implement the delay line, a good candidate is the one based on cascaded asymmetric Mach Zehnder Interferometers (aMZI) reported in [42]. This device is attractive since it can be easily reconfigured using thermo optic phase shifters, it is built using standard and robust optical components, and has a broadband spectral response. While an in-depth discussion lies out of the scope of this work, we only comment on the feasibility of the method. Following the results found in [42], the maximum delay ΔT is linked to the FSR of the aMZI as $\text{FSR}_\lambda = \frac{2\lambda^2}{c\Delta T}$. Using $\Delta T = 1.47$ ps, we have that $\text{FSR}_\lambda \sim 11$ nm, and the minimum 3 dB-bandwidth of the device transmittance is $\sim 1.27 \times \frac{\text{FSR}_\lambda}{2} \sim 7$ nm [42]. This should be sufficiently large to transmit the pump, the signal and the idler photons without significant distortions of their temporal wavepackets.

5. Influence of SPM and XPM on the source tunability

In our scheme, we use sub-ps pulses of high peak power (~ 10 W for 1 mW of average power) to compensate the large effective area of the FWM interaction. It is well known that SPM and XPM, triggered by the high power intensities, influence the shape of the JSA [36,37,43,44]. In our case, the accumulated SPM of the pumps and their XPM on the signal/idler photons both depend on τ , because the delay determines the position along the waveguide where the two pump pulses overlap and the pair is generated. When $\tau \sim 0$, the SPM accumulated by the pumps is minimum, but the XPM induced on the photons is maximum. The opposite holds when $\tau \sim \tau_{\max}$. We numerically simulated these regimes, focusing in particular on how the pump power influences the maximum tuning range $\Delta\lambda_{s(i)}^{\max}$. In Fig. 5(a) we plot this quantity as a function of the average pump power and a tapering amplitude of $\Delta w = 0.25$ μm . The tuning range increases with the pump power, with the Idler photon being slightly more sensitive ($\sim 0.33 \frac{\text{nm}}{\text{mW}}$) than the signal ($\sim 0.26 \frac{\text{nm}}{\text{mW}}$) to power variations. Figure 5(b) shows $\Delta\lambda_{s(i)}$ as a function of $\frac{\tau}{\tau_{\max}}$ for different input

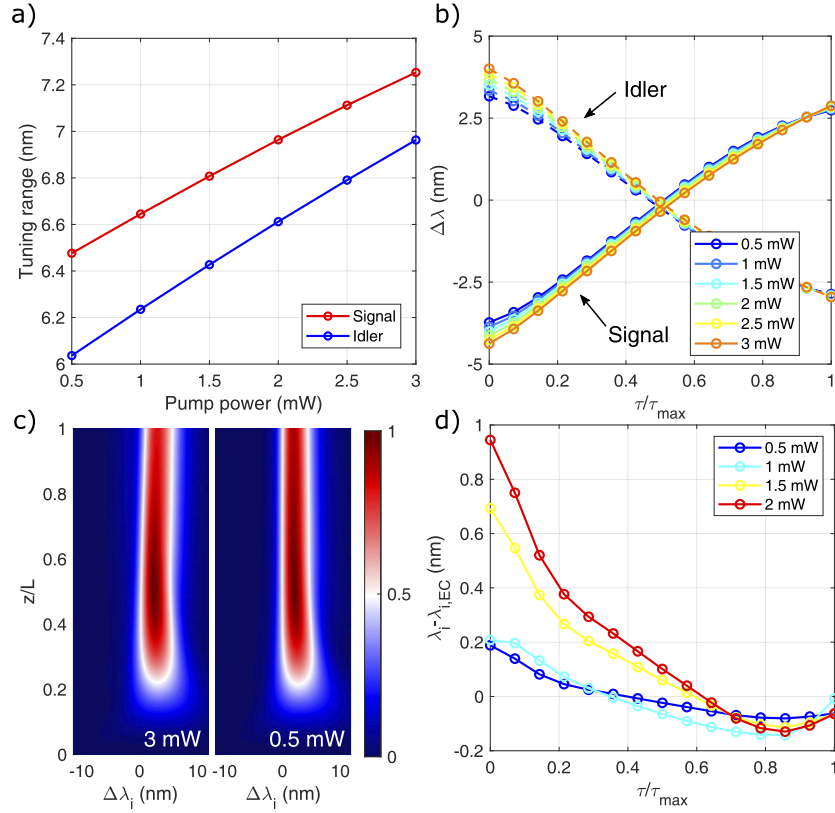


Fig. 5. (a) Maximum tuning range of the signal and of the idler wavelength as a function of the input pump power. (b) Shift of the signal and idler wavelength as a function of τ for different values of the input pump power. In both panels (a) and (b), the tapering amplitude is fixed to $\Delta w = 0.25 \mu\text{m}$. (c) Spectrally-resolved cumulative generation probability of the Idler photon as a function of the position along the waveguide. This quantity has been normalized to its maximum for clarity, so it has not to be interpreted as a true probability. The two plots refer to an input power of 3 mW (left) and 0.5 mW (right), while $\tau = 0.15\tau_{\max}$. (d) Deviation of the average idler wavelength λ_i with respect to the one predicted by energy conservation $\lambda_{i,EC}$. This quantity is shown as a function of τ and for different values of the input power.

powers. Nonlinear effects alter the wavelengths of the signal and the Idler especially at small delays, which suggests that they originate from XPM. As the pump power increases, the signal blue shifts from the low power condition, while the Idler red shifts. To better understand the origin of this phenomenon, we plot in Fig. 5(c) the spectrally-resolved cumulative probability to generate the Idler along the waveguide, which is obtained by marginalizing $\Phi(\omega_s, \omega_i, z)$ over ω_s . This is shown for $\frac{\tau}{\tau_{\max}} = 0.15$ in both the low power (0.5 mW) and the high power regime (3 mW). It is evident that, in both cases, Idlers are generated at approximately the same wavelength. We then observe a red shift and a spectral broadening of the Idler spectra only at high power. This is a clear signature that XPM and SPM are not affecting the phase matching condition, but rather that the spectral shift arises from XPM after that the pair is generated. This phenomenon, called XPM induced asymmetric spectral broadening, is well known to occur in optical fibers in presence of a temporal walk-off between an intense pump and a weak probe beam [34]. Since $\Delta\lambda_{s(i)}$ are modified by XPM after that the pair is generated, they do not obey the energy conservation

relation $\Delta\lambda_{i,EC} = -\left(\frac{\lambda_{i0}}{\lambda_{s0}}\right)^2 \Delta\lambda_{s,EC}$. This implies that any spectral distinguishability arising from XPM can not be recovered by changing the delay τ . In Fig. 5(d) we plot the discrepancy of the Idler wavelength λ_i from the one $\lambda_{i,EC}$ expected by energy conservation. To determine $\lambda_{i,EC}$, the pump wavelength is fixed and we use the average wavelength of the signal extracted from the JSA. At low power, the deviation is zero at $\tau = \frac{\tau_{max}}{2}$, while the small discrepancies at $\tau \rightarrow 0$ and $\tau \rightarrow \tau_{max}$ have exclusively to be attributed to the asymmetric marginal spectra of the Idler which arise from border effects (see Fig. 2(b)). Up to 1 mW, nonlinear effects still have a limited impact, with $|\lambda_i - \lambda_{i,EC}| \leq 0.1$ nm. At 2 mW, deviations from energy conservation can be as high as 1 nm at $\tau = 0$. However, as shown in Fig. 4(c), the delays which are used to correct the fabrication errors lie in the range $\tau \in (0.25, 0.7)$, and within this interval $|\lambda_i - \lambda_{i,EC}| \leq 0.3$ nm, which is less than 10% of the spectral linewidth of each photon. We then conclude that, up to 2 mW, XPM and SPM effects do not severely compromise the spectral indistinguishability. It is worth to note that the source is conceived to work in the low (e.g., $\xi < 0.1$) squeezing regime to limit multiphoton contamination in the heralded photon states [3]. Therefore, it is very unlikely that we will use input powers higher than 1 mW, since this level already corresponds to $\xi = 0.1$ (see Fig. 2(d)). As a comparison, we have that $\xi = 0.25$ at 2 mW of input power.

6. Conclusions

We proposed a scheme to generate highly pure and spectrally tunable photon pairs using delayed-pump Intermodal Four Wave Mixing. The high purity is inherited from the engineering of the phase matching relation and from the adiabatic switching of the nonlinear interaction. The tunability of the emission wavelength is added by tapering the width of the waveguide, and by changing the delay between the pump pulses. We demonstrate that the tunability range can be extended by increasing the tapering amplitude, with only a modest reduction in the purity of the heralded single photon states and with almost no impact on the pair generation probability. We show that, by optimizing the pump delay, we can drastically reduce the distinguishability among independent sources which arise from fabrication errors. Under realistic fabrication tolerances, an indistinguishability level $>95\%$ can be guaranteed up to a difference in the waveguide height of 4 nm, and for errors in the waveguide width larger than 100 nm. Under these circumstances, we predicted a degradation of the HHOM visibility of less than 3% of its value compared to the case of two identical sources. In comparison, the visibility and the indistinguishability will be both below 20% without delay optimization. We also show that, in the regime of low pair generation, XPM and SPM effects are not affecting the device performance. The proposed device can be built using standard integrated optical components provided by commercial photonic design kits and could be reconfigured using thermo optical phase shifters. Its implementation can mitigate indistinguishability issues either in large scale quantum photonic circuits encompassing arrays of sources, or in distant devices for quantum communication which are manufactured on different chips.

Appendix A: expressions for the linear and nonlinear momentum

The momentum flux M governing the spatial evolution along the waveguide length of each operator is defined as [35]:

$$M(z) = \int (\mathbf{D} \times \mathbf{B}) \cdot \hat{z} dx dy \sim \frac{1}{c} \int D_y^-(x, y, z, t) E_y^+(x, y, z, t) dx dy dt + \text{h.c.}, \quad (12)$$

where D^- and E^+ denote respectively the negative and the positive frequency part of the displacement and the electric field operator. The first involves only photon creation operators, while the second only annihilation operators (see the field expansion in Eq. (2)). In Eq. (12), we assumed that the \mathbf{E} field is entirely polarized along the y direction (TM modes), and that \mathbf{B} can be

expressed as $\mathbf{B} = \frac{1}{c}(E_y, 0, 0)$ (plane wave approximation). Then, one writes $D_y = \epsilon_0 n^2 E_y + P_y^{\text{NL}}$, where n is the material refractive index and P_y^{NL} is the nonlinear polarization, which in our case consists only in the term $P_y^{\text{NL}} = \epsilon_0 \chi_{yyyy}^{(3)} E_y^3$, where $\chi_{yyyy}^{(3)}$ is the isotropic contribution to the third order nonlinear susceptibility. In the next steps, one finds suitable expressions for $\mathbf{E}(x, y, z, t)$, as the ones in Eq. (2), insert them into Eq. (12), and separates the linear terms from the ones generated by the nonlinear polarization. This standard procedure can be found, e.g., in [45], hence we will only report the final result. The linear momentum M_L is given by [36,45]:

$$M_L = \int \hbar \beta(\omega) a^\dagger(\omega, z) a(\omega, z) d\omega. \quad (13)$$

Since the pump, the signal and the Idler fields are narrowband and centered into three non-overlapping frequency ranges, the integral in Eq. (13) can be split into $M_L = M_L^p + M_L^s + M_L^i$. Each term has the same form of Eq. (13), but with the integral restricted to the frequency range of the corresponding beam. Within these intervals, one can define the slowly varying operators (see Eq. (2)) $\tilde{a}_q(z, \omega_q) = a(\omega_q + \bar{\omega}_q, z) e^{-i\bar{\beta}_q z}$, where $q = \{p, s, i\}$. By Taylor expanding the wavevector β up to the second order in the frequency detuning $(\omega - \bar{\omega})$ in Eq. (13), we have:

$$M_L = \sum_{q=\{p,s,i\}} \hbar \int (\bar{\beta}_q + v_q(\omega_q - \bar{\omega}_q) + \frac{\beta_q^{(2)}}{2}(\omega_q - \bar{\omega}_q)^2) \tilde{a}_q^\dagger(\omega_q - \bar{\omega}_q, z) \tilde{a}_q(\omega_q - \bar{\omega}_q, z) d\omega_q, \quad (14)$$

Table 1. Values of the parameters used in the simulation of the JSA and JTA through this work.

Parameter	Value
α_{p1}	0.4 dB/cm
α_{p2}	0.2 dB/cm
v_{p1}	75.20 $\mu\text{m}/\text{ps}$
v_{p2}	73.41 $\mu\text{m}/\text{ps}$
v_s	75.29 $\mu\text{m}/\text{ps}$
v_i	73.5 $\mu\text{m}/\text{ps}$
L_{wp}	0.25 cm
$ L_{ws} $	3.27 cm
$ L_{wi} $	0.26 cm
L_{Dp1}	4.60 cm
L_{Dp2}	4.43 cm
L_{Ds}	4.09 cm
L_{Di}	5.18 cm
γ_{1111}	2.73 $\frac{1}{\text{m}\cdot\text{W}}$
$\gamma_{1122} = \gamma_{2211}$	1.77 $\frac{1}{\text{m}\cdot\text{W}}$
γ_{2222}	2.60 $\frac{1}{\text{m}\cdot\text{W}}$
γ_{11ss}	1.52 $\frac{1}{\text{m}\cdot\text{W}}$
γ_{22ss}	2.25 $\frac{1}{\text{m}\cdot\text{W}}$
γ_{11ii}	3.12 $\frac{1}{\text{m}\cdot\text{W}}$
γ_{22ii}	2.01 $\frac{1}{\text{m}\cdot\text{W}}$
γ_{p1p2si}	1.34 $\frac{1}{\text{m}\cdot\text{W}}$

where $\beta_q^{(2)} = \frac{d^2\beta_q}{d\omega^2}$. The SPM, XPM and FWM terms are more easily expressed in the time domain, where they have the following form [36]:

$$\begin{aligned} M_{\text{SPM}} &= \frac{1}{2}\hbar \sum_{q=\{p_1, p_2\}} \gamma_{qqqq} \int |\tilde{A}_q(z, t)|^2 \tilde{A}_q(z, t) dt, \\ M_{\text{XPM}} &= 2\hbar \sum_{q=\{p_1, p_2\}} \sum_{r=\{s, i\}} \gamma_{qqrr} |\tilde{A}_q(z, t)|^2 \tilde{A}_r(z, t) dt, \\ M_{\text{FWM}} &= \hbar \gamma_{p_1 p_2 s i} \int \tilde{A}_{p_1}(z, t) \tilde{A}_{p_2}(z, t) \tilde{a}_s^\dagger(z, t) \tilde{a}_i^\dagger(z, t) dt. \end{aligned} \quad (15)$$

The definitions in Eq. (15) make use of the nonlinear parameter $\gamma_{ijkl} = \frac{\omega n_2}{c A_{ijkl}}$, where n_2 is the nonlinear refractive index of silicon and A_{ijkl} is the nonlinear effective area, defined as:

$$A_{ijkl} = \frac{\prod_{q=\{i, j, k, l\}} \left(\int |F_q(x, y)|^2 dx dy \right)^{\frac{1}{2}}}{\int_{\text{wg}} F_i(x, y) F_j(x, y) F_k(x, y)^* F_l(x, y)^* dx dy}. \quad (16)$$

The values of the parameters introduced so far and the ones appearing in Eq. (3–7) are calculated using the commercial Lumerical MODE package [46], and are listed in Table 1. Losses are taken from the measured values in [27].

Appendix B: derivation of the propagation equation for the JTA

We start from the definition of the JTA given in Section 2, that we rewrite here for clarity:

$$\Phi(T_s, T_i, z) = \langle \tilde{a}_s(T_s, z) \tilde{a}_i(T_i, z) U(z, 0) \rangle. \quad (17)$$

By performing the derivative in z of both members in Eq. (17) we get:

$$\frac{\partial \Phi}{\partial z} = \left\langle \frac{\partial \tilde{a}_s}{\partial z} \tilde{a}_i U + \tilde{a}_s \frac{\partial \tilde{a}_i}{\partial z} U \right\rangle + \langle \tilde{a}_s \tilde{a}_i \frac{\partial U}{\partial z} \rangle. \quad (18)$$

We now use Eq. (5) to express $\frac{\partial \tilde{a}_{s(i)}}{\partial z} = (L'_{s(i)} + N_{s(i)}) \tilde{a}_{s(i)}$, where $L'_{s(i)} = L_{s(i)} + i\Delta\beta_{s(i)}(z)$ and the definition of the operators $L_{s(i)}$ and $N_{s(i)}$ are given in Eq. (7). Moreover, from Section 2 we have that $\frac{\partial U}{\partial z} = \frac{i}{\hbar} M_{\text{FWM}}$, so as Eq. (18) becomes:

$$\frac{\partial \Phi}{\partial z} = \langle [(L'_s + N_s) \tilde{a}_s] \tilde{a}_i U \rangle + \langle \tilde{a}_s [(L'_i + N_i) \tilde{a}_i] U \rangle + \frac{i}{\hbar} \langle \tilde{a}_s \tilde{a}_i M_{\text{FWM}} \rangle. \quad (19)$$

The first two terms on the right hand side have exactly the same form, so we will only treat the case of the signal and apply the same result to the Idler. Writing $\tilde{a}_s(T_s, z)$ using its Fourier Transform:

$$\tilde{a}_s(T_s, z) = \int \tilde{a}_s(\omega'_s, z) e^{-iT_s \omega'_s} d\omega'_s, \quad (20)$$

the application of L'_s replaces \tilde{a}_s by $\tilde{a}_s \rightarrow f(\omega'_s) \tilde{a}_s = (-\alpha_s/2 + i\Delta\beta_s \omega'_s/L_{w_s} + i\omega_s'^2/(2L_{D_s})) \tilde{a}_s$. By writing also \tilde{a}_i using its Fourier Transform, we have:

$$\langle [(L'_s + N_s) \tilde{a}_s] \tilde{a}_i U \rangle = \int f(\omega'_s) e^{-iT_s \omega'_s} e^{-iT_i \omega'_i} \langle \tilde{a}_s(\omega'_s, z) \tilde{a}_i(\omega'_i, z) U \rangle d\omega'_s d\omega'_i. \quad (21)$$

The expectation value on the right hand side is the definition of the JSA $\tilde{\Phi}(\omega'_s, \omega'_i, z)$. Following an identical procedure for the Idler, we have that:

$$\langle [L'_s \tilde{a}_s] \tilde{a}_i U + \tilde{a}_s [L'_i \tilde{a}_i] U \rangle = \int [f(\omega'_s) + f(\omega'_i)] e^{-iT_s \omega'_s} e^{-iT_i \omega'_i} \tilde{\Phi}(\omega'_s, \omega'_i, z) d\omega'_s d\omega'_i, \quad (22)$$

which is equivalent to apply the operator $L'_{s(i)}$ to the JTA. In the time domain, the operator $N_{s(i)}$ is simply a multiplicative factor, so we have that $\langle N_{s(i)} \tilde{a}_s \tilde{a}_i U \rangle = N_{s(i)} \langle \tilde{a}_s \tilde{a}_i U \rangle = N_{s(i)}(T_{s(i)}) \Phi(T_s, T_i, z)$.

By combining this result with the expression in Eq. (22), the first two terms on the right hand side of Eq. (19) becomes $\langle [(L'_s + N_s)\tilde{a}_s]\tilde{a}_i U \rangle + \langle \tilde{a}_s[(L'_i + N_i)\tilde{a}_i]U \rangle = (L'_s + L'_i + N_s + N_i)\Phi(T_s, T_i, z)$. We now work out the driving term $\langle \tilde{a}_s\tilde{a}_i M_{\text{FWM}} \rangle$ in the frequency domain. By using Eq. (20), we have:

$$\frac{i}{\hbar} \langle \tilde{a}_s\tilde{a}_i M_{\text{FWM}} \rangle = i\gamma_{p_1 p_2 s i} \int A_{p_1}(t, z) A_{p_2}(t, z) \langle \tilde{a}_s(\omega_s, z) \tilde{a}_s(\omega_i, z) \tilde{a}_s^\dagger(\omega'_s, z) \tilde{a}_i^\dagger(\omega'_i, z) \rangle \times, \quad (23)$$

$$e^{-i(T_s\omega_s + T_i\omega_i)} e^{iT(\omega'_s + \omega'_i)} dt d\omega_s d\omega'_s d\omega_i d\omega'_i.$$

Using the equal space commutation relations $[a(\omega, z), a^\dagger(\omega', z)] = \delta(\omega - \omega')$, the expectation value in Eq. (23) gives $\delta(\omega_s - \omega'_s)\delta(\omega_i - \omega'_i)$. After integration in ω_s and ω_i , we have $\omega_s = \omega'_s$ and $\omega_i = \omega'_i$. Then, in the frequency domain, the product of the pump envelopes is $A_{p_1}(t, z)A_{p_2}(t, z) = \int \mathcal{A}_{p_1}(x', z)\mathcal{A}_{p_2}(x - x', z)e^{ixt} dx dx'$, which inserted into Eq. (23) gives:

$$\frac{i}{\hbar} \langle \tilde{a}_s\tilde{a}_i M_{\text{FWM}} \rangle = i\gamma_{p_1 p_2 s i} \int \mathcal{A}_{p_1}(x, z)\mathcal{A}_{p_2}(x - x', z) e^{it(\omega'_s + \omega'_i - x)} e^{-i(T_s\omega'_s + T_i\omega'_i)} d\omega'_s d\omega'_i dt dx dx'. \quad (24)$$

Integration over t gives $\delta(\omega'_s + \omega'_i - x)$, and a subsequent integration over x sets $x = \omega'_s + \omega'_i$. Expression Eq. (24) reduces to:

$$\frac{i}{\hbar} \langle \tilde{a}_s\tilde{a}_i M_{\text{FWM}} \rangle = e^{i \int_0^z (\Delta\beta_{p_1}(z') + \Delta\beta_{p_2}(z')) dz'} \int G(\omega'_s, \omega'_i, z) e^{-i(T_s\omega'_s + T_i\omega'_i)} d\omega'_s d\omega'_i, \quad (25)$$

where $G = i \int \mathcal{A}_{p_1}(x, z)\mathcal{A}_{p_2}(\omega'_s + \omega'_i - x, z) dx$ and we wrote the pump as $\mathcal{A}_{p_1(2)}(x, z) = \mathcal{A}_{p_1(2)}(x, z) \exp\left(i \int_0^z \Delta\beta_{p_1(2)}(z') dz'\right)$ to factor out the effect of tapering. As a final step, in order to recover Eq. (7) of the main text, we write $\Phi(T_s, T_i, z) = \tilde{\Phi}(T_s, T_i, z) e^{i\Theta_{si}(z)}$, where Θ_{si} is defined in Eq. (7), and we use the fact that $\frac{\partial \Theta_{si}}{\partial z} = (\Delta\beta_s + \Delta\beta_i)$ cancels the $\Delta\beta$ terms in the operators $L'_{s(i)}$.

Appendix C: analytic expression for the cumulative pair generation probability

Here we derive an analytic expression for the evolution of the cumulative pair generation probability along the waveguide, in the approximation of zero loss, SPM, XPM and group velocity dispersion. In this scenario, Eq. (8) reduces to $\xi(z) = 2 \int_0^z \mathcal{R}[S\Phi^*]$. By using the expression of S in Eq. (7), we get:

$$\xi(z) = 2 \int_0^z \mathcal{R} [A_{p_1}(z', t) A_{p_2}(z', t) \Phi^* \exp(it(\omega'_s + \omega'_i) - T_s\omega'_s - T_i\omega'_i) d\omega'_s d\omega'_i dT_s dT_i dz' dt], \quad (26)$$

where we have used $\int \mathcal{A}_{p_1}(x, z)\mathcal{A}_{p_2}(\omega'_s + \omega'_i - x, z) dx = \int A_{p_1}(t, z) A_{p_2}(t, z) e^{it(\omega'_s + \omega'_i)} dt$. The phase mismatch $e^{i\Theta}$ term in Eq. (7) has been assumed to be ~ 1 in the region where the product of the pump envelopes is $\neq 0$. We now integrate the exponential in the two variables ω'_s and ω'_i to obtain the product of the Dirac delta $\delta(t - T_s)\delta(t - T_i)$, which is not vanishing only when $T_s = T_i = t$. Hence Eq. (26) reduces to:

$$\xi(z) = 2 \int_0^z \mathcal{R} [A_{p_1}(t, z') A_{p_2}(t, z') \Phi(T_s = t, T_i = t, z')^*] dz' dt. \quad (27)$$

In absence of group velocity dispersion, XPM and SPM, we have that $\Phi \propto A_{p_1}(t_c, z_c) A_{p_2}(t_c, z_c)$, in which t_c and z_c define the collision time and the collision coordinate of the pair generation event [37,39,40]. These are given by:

$$z_c = L - \frac{T_0(T_s - T_i)}{v_s^{-1} - v_i^{-1}}, \quad t_c = \frac{v_s^{-1} T_i - v_i^{-1} T_s}{v_s^{-1} - v_i^{-1}}. \quad (28)$$

From these definitions, we see that when $T_s = T_i = t$, the collision coordinates are $z_c = L$ and $t_c = t$. From a physical point of view, this reflects the fact that pairs are generated at the

same time but they possess different group velocities. Hence, in order to be detected at the same time, the collision coordinate should coincide with the end of the waveguide. Using these results, Eq. (27) becomes:

$$\xi(z) \propto \int_0^z |A_{p1}(z', t)|^2 |A_{p2}(z', t)|^2 dz' dt. \quad (29)$$

We can evaluate the time integral in Eq. (29) by moving off from the pump reference frame, in which the pump envelopes have expression $A_{p1} = \bar{A}_{p1} e^{-\frac{z-v_1(t-\tau)}{2\sigma_1^2}}$ and $A_{p2} = \bar{A}_{p2} e^{-\frac{z-v_2 t}{2\sigma_2^2}}$, where $\sigma_{1(2)}$ are given by $\sigma_{1(2)} = \frac{v_{1(2)} T_0}{2\sqrt{\ln 2}}$ and $|\bar{A}_{p1(2)}|^2$ is the peak power of the pulses. After the time integral, the result is a gaussian function centered at $z = L_{\text{match}} = \tau \left(\frac{1}{v_2} - \frac{1}{v_1} \right) = \frac{\tau}{\tau_{\text{max}}} L$ and with standard deviation σ_z :

$$\sigma_z = \frac{\sqrt{v_2^2 \sigma_1^2 + v_1^2 \sigma_2^2}}{v_1^2 - v_2^2} = \frac{L_{wp}}{2\sqrt{\ln 2}}, \quad (30)$$

which is the result of the main text. Therefore:

$$\xi(z) \propto \int_0^z e^{-\frac{(z'-L_{\text{match}})^2}{2\sigma_z^2}} dz' \propto \text{erf} \left(\frac{z - L_{\text{match}}}{\sqrt{2}\sigma_z} \right). \quad (31)$$

Funding. Horizon 2020 Framework Programme (EC 899368, EPIQUS).

Acknowledgments. This project has received funding from the European Union's Horizon 2020 research and innovation programme under grant agreement No 899368.

Disclosures. The authors declare no conflicts of interest.

Data availability. Data underlying the results presented in this paper are not publicly available at this time but may be obtained from the authors upon reasonable request.

References

1. L. Caspani, C. Xiong, B. J. Eggleton, D. Bajoni, M. Liscidini, M. Galli, R. Morandotti, and D. J. Moss, "Integrated sources of photon quantum states based on nonlinear optics," *Light: Sci. Appl.* **6**(11), e17100 (2017).
2. J. Wang, F. Sciarrino, A. Laing, and M. G. Thompson, "Integrated photonic quantum technologies," *Nat. Photonics* **14**(5), 273–284 (2020).
3. D. Bonneau, G. J. Mendoza, J. L. O'Brien, and M. G. Thompson, "Effect of loss on multiplexed single-photon sources," *New J. Phys.* **17**(4), 043057 (2015).
4. M. J. Collins, C. Xiong, I. H. Rey, T. D. Vo, J. He, S. Shahnia, C. Reardon, T. F. Krauss, M. Steel, A. S. Clark, and B. J. Eggleton, "Integrated spatial multiplexing of heralded single-photon sources," *Nat. Commun.* **4**(1), 2582 (2013).
5. J. J. Renema, A. Menssen, W. R. Clements, G. Triginer, W. S. Kolthammer, and I. A. Walmsley, "Efficient classical algorithm for boson sampling with partially distinguishable photons," *Phys. Rev. Lett.* **120**(22), 220502 (2018).
6. V. Shchesnovich, "Sufficient condition for the mode mismatch of single photons for scalability of the boson-sampling computer," *Phys. Rev. A* **89**(2), 022333 (2014).
7. C. Sparrow, "Quantum interference in universal linear optical devices for quantum computation and simulation," PhD Thesis (2017).
8. S. Signorini and L. Pavesi, "On-chip heralded single photon sources," *AVS Quantum Sci.* **2**(4), 041701 (2020).
9. S. Paesani, Y. Ding, R. Santagati, L. Chakhmakhchyan, C. Vigliar, K. Rottwitt, L. K. Oxenløwe, J. Wang, M. G. Thompson, and A. Laing, "Generation and sampling of quantum states of light in a silicon chip," *Nat. Phys.* **15**(9), 925–929 (2019).
10. J. Arrazola, V. Bergholm, K. Brádler, T. Bromley, M. Collins, I. Dhand, A. Fumagalli, T. Gerrits, A. Goussev, L. Helt, J. Hundal, T. Isacsson, R. B. Israel, J. Izaac, S. Jahangiri, R. Janik, N. Killoran, S. Kumar, J. Lavoie, A. E. Lita, D. H. Mahler, M. Menotti, B. Morrison, S. W. Nam, L. Neuhaus, H. Y. Qi, N. Quesada, A. Repington, K. K. Sabapathy, M. Schuld, D. Su, J. Swinerton, A. Száva, K. Tan, P. Tan, V. D. Vaidya, Z. Vernon, Z. Zabaneh, and Y. Zhang, "Quantum circuits with many photons on a programmable nanophotonic chip," *Nature* **591**(7848), 54–60 (2021).
11. C. Vigliar, S. Paesani, Y. Ding, J. C. Adcock, J. Wang, S. Morley-Short, D. Bacco, L. K. Oxenløwe, M. G. Thompson, J. G. Rarity, and A. Laing, "Error-protected qubits in a silicon photonic chip," *Nat. Phys.* **17**(10), 1137–1143 (2021).
12. S. Bartolucci, P. Birchall, H. Bombin, H. Cable, C. Dawson, M. Gimeno-Segovia, E. Johnston, K. Kieling, N. Nickerson, M. Pant, F. Pastawski, T. Rudolph, and C. Sparrow, "Fusion-based quantum computation," arXiv preprint arXiv:2101.09310 (2021).

13. J. C. Adcock, S. Morley-Short, J. W. Silverstone, and M. G. Thompson, "Hard limits on the postselectability of optical graph states," *Quantum Sci. Technol.* **4**(1), 015010 (2018).
14. J. C. Adcock, C. Vigliar, R. Santagati, J. W. Silverstone, and M. G. Thompson, "Programmable four-photon graph states on a silicon chip," *Nat. Commun.* **10**(1), 3528 (2019).
15. D. Llewellyn, Y. Ding, I. I. Faruque, S. Paesani, D. Bacco, R. Santagati, Y.-J. Qian, Y. Li, Y.-F. Xiao, M. Huber, M. Malik, G. F. Sinclair, X. Zhou, K. Rottwitt, J. L. O'Brien, J. Rarity, Q. Gong, L. K. Oxenlowe, J. Wang, and M. G. Thompson, "Chip-to-chip quantum teleportation and multi-photon entanglement in silicon," *Nat. Phys.* **16**(2), 148–153 (2020).
16. F. Graffitti, P. Barrow, M. Proietti, D. Kundys, and A. Fedrizzi, "Independent high-purity photons created in domain-engineered crystals," *Optica* **5**(5), 514–517 (2018).
17. B. M. Burridge, I. I. Faruque, J. G. Rarity, and J. Barreto, "High spectro-temporal purity single-photons from silicon micro-racetrack resonators using a dual-pulse configuration," *Opt. Lett.* **45**(14), 4048–4051 (2020).
18. Y. Liu, C. Wu, X. Gu, Y. Kong, X. Yu, R. Ge, X. Cai, X. Qiang, J. Wu, X. Yang, and P. Xu, "High-spectral-purity photon generation from a dual-interferometer-coupled silicon microring," *Opt. Lett.* **45**(1), 73–76 (2020).
19. D. R. Blay, M. Steel, and L. Helt, "Effects of filtering on the purity of heralded single photons from parametric sources," *Phys. Rev. A* **96**(5), 053842 (2017).
20. S. Y. Siew, B. Li, F. Gao, H. Y. Zheng, W. Zhang, P. Guo, S. W. Xie, A. Song, B. Dong, L. W. Luo, C. Li, X. Luo, and G. Q. Lo, "Review of silicon photonics technology and platform development," *J. Lightwave Technol.* **39**(13), 4374–4389 (2021).
21. J. W. Silverstone, R. Santagati, D. Bonneau, M. J. Strain, M. Sorel, J. L. O'Brien, and M. G. Thompson, "Qubit entanglement between ring-resonator photon-pair sources on a silicon chip," *Nat. Commun.* **6**(1), 7948 (2015).
22. E. Meyer-Scott, N. Montaut, J. Tiedau, L. Sansoni, H. Herrmann, T. J. Bartley, and C. Silberhorn, "Limits on the heralding efficiencies and spectral purities of spectrally filtered single photons from photon-pair sources," *Phys. Rev. A* **95**(6), 061803 (2017).
23. R. Kumar, J. R. Ong, J. Recchio, K. Srinivasan, and S. Mookherjee, "Spectrally multiplexed and tunable-wavelength photon pairs at 1.55 μm from a silicon coupled-resonator optical waveguide," *Opt. Lett.* **38**(16), 2969–2971 (2013).
24. R.-B. Jin, R. Shimizu, K. Wakui, H. Benichi, and M. Sasaki, "Widely tunable single photon source with high purity at telecom wavelength," *Opt. Express* **21**(9), 10659–10666 (2013).
25. D. Zhu, C. Chen, M. Yu, L. Shao, Y. Hu, C. Xin, M. Yeh, S. Ghosh, L. He, C. Reimer, N. Sinclair, F. N. C. Wong, M. Zhang, and M. Loncar, "Spectral control of nonclassical light using an integrated thin-film lithium niobate modulator," arXiv preprint arXiv:2112.09961, (2021).
26. Q. Li, M. Davanço, and K. Srinivasan, "Efficient and low-noise single-photon-level frequency conversion interfaces using silicon nanophotonics," *Nat. Photonics* **10**(6), 406–414 (2016).
27. S. Paesani, M. Borghi, S. Signorini, A. Mañón, L. Pavesi, and A. Laing, "Near-ideal spontaneous photon sources in silicon quantum photonics," *Nat. Commun.* **11**(1), 2505 (2020).
28. S. Signorini, M. Mancinelli, M. Borghi, M. Bernard, M. Ghulinyan, G. Pucker, and L. Pavesi, "Intermodal four-wave mixing in silicon waveguides," *Photonics Res.* **6**(8), 805–814 (2018).
29. S. Signorini, M. Sanna, S. Piccione, M. Ghulinyan, P. Tidemand-Lichtenberg, C. Pedersen, and L. Pavesi, "A silicon source of heralded single photons at 2 μm ," *APL Photonics* **6**(12), 126103 (2021).
30. A. Christ, K. Laiho, A. Eckstein, K. N. Cassemiro, and C. Silberhorn, "Probing multimode squeezing with correlation functions," *New J. Phys.* **13**(3), 033027 (2011).
31. J. G. Koefoed, J. B. Christensen, and K. Rottwitt, "Effects of noninstantaneous nonlinear processes on photon-pair generation by spontaneous four-wave mixing," *Phys. Rev. A* **95**(4), 043842 (2017).
32. G. P. Agrawal, P. Baldeck, and R. Alfano, "Temporal and spectral effects of cross-phase modulation on copropagating ultrashort pulses in optical fibers," *Phys. Rev. A* **40**(9), 5063–5072 (1989).
33. M. Karlsson, "Four-wave mixing in fibers with randomly varying zero-dispersion wavelength," *J. Opt. Soc. Am. B* **15**(8), 2269–2275 (1998).
34. G. P. Agrawal, "Nonlinear fiber optics," *Nonlinear Science at the Dawn of the 21st Century* (Springer, 2000), pp. 195–211.
35. B. Huttner, S. Serulnik, and Y. Ben-Aryeh, "Quantum analysis of light propagation in a parametric amplifier," *Phys. Rev. A* **42**(9), 5594–5600 (1990).
36. G. F. Sinclair and M. G. Thompson, "Effect of self-and cross-phase modulation on photon pairs generated by spontaneous four-wave mixing in integrated optical waveguides," *Phys. Rev. A* **94**(6), 063855 (2016).
37. B. Bell, A. McMillan, W. McCutcheon, and J. Rarity, "Effects of self-and cross-phase modulation on photon purity for four-wave-mixing photon pair sources," *Phys. Rev. A* **92**(5), 053849 (2015).
38. L. Helt, M. Steel, and J. Sipe, "Spontaneous parametric downconversion in waveguides: what's loss got to do with it?" *New J. Phys.* **17**(1), 013055 (2015).
39. J. G. Koefoed and K. Rottwitt, "Complete evolution equation for the joint amplitude in photon-pair generation through spontaneous four-wave mixing," *Phys. Rev. A* **100**(6), 063813 (2019).
40. J. G. Koefoed, S. M. Friis, J. B. Christensen, and K. Rottwitt, "Spectrally pure heralded single photons by spontaneous four-wave mixing in a fiber: reducing impact of dispersion fluctuations," *Opt. Express* **25**(17), 20835–20849 (2017).

41. S. K. Selvaraja, W. Bogaerts, P. Dumon, D. Van Thourhout, and R. Baets, "Subnanometer linewidth uniformity in silicon nanophotonic waveguide devices using cmos fabrication technology," *IEEE J. Sel. Top. Quantum Electron.* **16**(1), 316–324 (2009).
42. A. Waqas, D. Melati, and A. Melloni, "Cascaded mach–zehnder architectures for photonic integrated delay lines," *IEEE Photonics Technol. Lett.* **30**(21), 1830–1833 (2018).
43. J. B. Christensen, C. McKinstrie, and K. Rottwitt, "Temporally uncorrelated photon-pair generation by dual-pump four-wave mixing," *Phys. Rev. A* **94**(1), 013819 (2016).
44. Z. Vernon and J. Sipe, "Strongly driven nonlinear quantum optics in microring resonators," *Phys. Rev. A* **92**(3), 033840 (2015).
45. N. Quesada, L. Helt, M. Menotti, M. Liscidini, and J. Sipe, "Beyond photon pairs: Nonlinear quantum photonics in the high-gain regime," arXiv preprint arXiv:2110.04340 (2021).
46. <http://www.ansys.com>.